International Journal of Applied Research in Mechanical Engineering

Volume 2 | Issue 4 Article 2

April 2013

FRICTION STIR SURFACING OF COLD SPRAYED BAINITIC STEEL

P. VENKATESWARAN
Corporate Technology, Research and Technology Centre, Siemens Technology and Services Private Limited #84, Keonics Electronic City Bangalore 560100, India, venkateswaran.p@siemens.com

ANANT KUMAR MISHRA
Corporate Technology, Research and Technology Centre, Siemens Technology and Services Private Limited #84, Keonics Electronic City Bangalore 560100, India, anant.mishra@siemens.com

FRICTION STIR SURFACING OF COLD SPRAYED BAINITIC STEEL

VENKATESWARAN P[1], ANANT KUMAR MISHRA[2]

[1,2]Corporate Technology, Research and Technology Centre, Siemens Technology and Services Private Limited
#84, Keonics Electronic City Bangalore 560100, India
E-mail: venkateswaran.p@siemens.com, anant.mishra@siemens.com

Abstract- A superficial composite layer was produced by friction stir surfacing (FSS) on high strength bainitic steel, cold sprayed with the Cu-Y_2O_3-ZrO_2 and Zn-Y_2O_3-ZrO_2 metal-oxide powders. The FSS resulted consolidation of the elemental powders in the cold sprayed (CS) layer with some melting of Zn and Cu. The formation of a continuous, adherent layer on the steel surface facilitates closing of large pores at the coating-substrate interface. The consolidated layer on the steel surface showed comminution of the coarse oxide particles and concomitant reduction in the average particle size. The FSS resulted in a composite layer consisting of the hard martensite structure up to 0.4 mm from the surface. The region just below the top solidified layer exhibited the soft ferrite and pearlite structure with narrow microstructural bands of fine martensite. The net torque and in-plane forces for the composite layer production are significantly different from the Zn and Cu cold sprayed layers.

Keywords- *Friction stir surfacing, Cold spray, Friction, Composite, Bainitic steel*

I. INTRODUCTION

Functional coatings for high temperature applications such as thermal barrier coating on the turbine blades, vanes and discs or the coatings for electrical conductors are produced using high energy, thermal processes such as plasma spray, high velocity oxy-fuel (HVOF), laser cladding and the hard facing. These methods often result in significantly high levels of porosity, high residual stress and an adverse effect on the substrate due to high temperature levels involved in these methods. Cold gas dynamic spray (or simply cold spray) is a process of applying coatings by exposing a metallic or dielectric substrate to a high velocity (300-1200 m/s) jet of small particles (1-50 □m) particles accelerated by a supersonic jet of compressed gas. In the cold spray (CS) process, powder particles are accelerated by the supersonic gas jet (deLaval type nozzle) at a temperature that is always lower than the melting point of the materials involved, resulting in coating formation from the solid state particles [1]. The cold spray process has several advantages such as low levels of oxidation, properties degradation of the substrate, evaporation and residual stress compared to thermal spray processes.

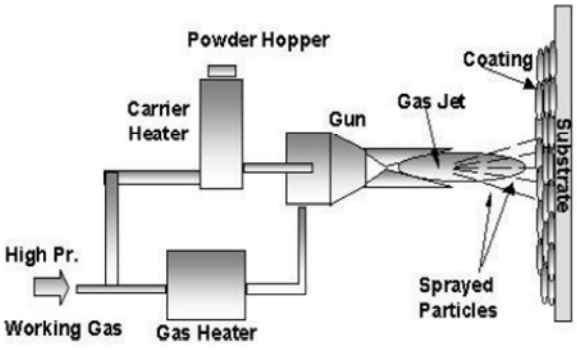

Fig. 1. Schematic of the cold spray process set up

Several reports have explained the successful application of the cold spray process for spraying of metal-oxides composite powders on the metal surface [2-4]. The schematic of the cold spray process is shown in Fig. 1 [4]. Despite several advantages, the adherence between the top coat and the substrate of the cold spray process may not be sufficient for high end application, particularly for hard metal oxides to satisfy the stringent service requirements like the high temperature stability, wear resistance, thermal and electrical conductivity, surface finish in turbines, electrical contacts and heavy structural parts like rolls, bearing etc. The distribution of the particulates inside the cold sprayed layer, in case of the metal-oxide coatings may not be uniform. In such cases, the homogenization of the CS layer, hence the bond strength and the uniform distribution of the particulates is necessary to get a homogenized microstructure inside the cold spray zone. Friction Stir Surfacing (FSS) can be used to densify the CS surfaces owing to its eco-friendly, solid-state process. The FSS is a variant of the friction stir welding (FSW) process, where the profiled tool is used to weld the plates to be joined together. The schematic of the FSW process is shown in Fig. 2. The welding takes place by the heat generation due to the dissipation of the plastic work during the penetration of the rotating tool inside the plates to be joined [5]. In FSS the rotating tool is plunged into the top surface of the metal workpiece, which contains loosely deposited powders or the sprayed coatings from thermal or cold spray processes. The plunge depth can be set to a pre-defined value which can be shorter than the workpiece thickness. The resulting surface is the composite layer which domiciles multiple metallic and the oxide particles. The benefits of the CS and FSS together can be applied to enable the reuse of the damaged components. The several reports of efforts of the cold spraying and the friction

stir surfacing as individual processes are available in the open literature [2-7]. However, the effect of the FSS on the CS steel surfaces is not available, despite its potential to be used as environmental friendly surface modification process. The present work is an attempt to demonstrate the feasibility of particulate composite manufacturing at superficial layers of high strength steel. The cold sprayed Cu-Y_2O_3-ZrO_2 and Zn-Y_2O_3-ZrO_2 layers on bainitic steel were friction stir surfaced using the computer controlled friction stir welding system. The key process response variables namely, vertical force (F_z) in-plane forces (F_r), and torque for producing good quality FSS layers are captured. The details of the microstructural changes and the corresponding hardness data due to CS and FSS are presented.

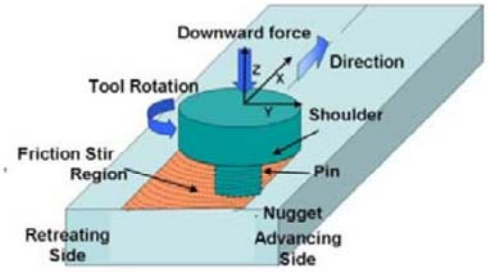

Fig. 2. Schematic of the friction stir surfacing process [6]

II. EXPERIMENTS AND PROCEDURES

A. Base Material and properties

The substrate used was a low carbon, Cr-Mo steel (ASTM A387 Grade 5) of 6.4 mm thickness. The chemical composition of the steel plate was determined using the inductively coupled plasma (ICP) optical emission spectroscopy (OES) except for the carbon. The chemical composition of the steel is presented in Table 1.

Table I. Chemical composition (wt. %) of the steel substrate

C	Mn	Si	Cr	Mo	Cu	S&P
0.12	0.54	0.72	1.14	0.45	0.13	0.001

Tensile properties of the steel plates (samples S1 and S2) were performed as per ASTM E8 [8] standard with specimens of 50 mm gauge length. The yield strength (YS), ultimate tensile strength (UTS) and elongation of the steel is presented in Table 2.

Table II. Tensile properties of the base metal

Sample	YS (MPa)	UTS (MPa)	Elongation (%)
S1	584	678	22
S2	589	689	22

B. Cold spray (CS) process

Cold spraying on the steel plates was performed at The International Advanced Research Centre for Powder Metallurgy and New Materials (ARCI), Hyderabad. The indigenously developed cold spray unit at ARCI was for preparing the coating. The robotic assisted CS gun was used to ensure the uniformity in the coating. The process conditions used for the Cu-Y_2O_3-ZrO_2 and Zn-Y_2O_3-ZrO_2 are presented in Table 3.

Table III. The cold spray parameters

Coating	Precursor Composition (wt.%)	Y_2O_3-ZrO_2 size (μ)	Pressure (bar)	Gas pre-heating Temperature (°C)
Cu-Y_2O_3-ZrO_2	50 oxides:50 metal	20-120	9	500
Zn-Y_2O_3-ZrO_2	50 oxides:50 metal	20-120	9	350

The metallic Cu and Zn have minimum 95% of particles having < 44 microns (-325 mesh) and the Y_2O_3-ZrO_2 particles have the range of 20-120 microns. The plates were grit blasted before the CS process to remove the continuous oxide film on the steel surface and to enhance the coating-substrate bonding.

C. Friction stir surfacing (FSS) process

Friction stir surfacing of the cold sprayed plates were performed using the 67 kN capacity, Manufacturing Technologies Inc. (MTI) friction stir welder available at Jadavpur University, Kolkata. Fig. 3 shows the picture of the equipment and tool at the inset. The water cooled polycrystalline boron nitride (PCBN) was used for the FSS experiments.

The tool shoulder and pin diameters are 36.5 mm and 5 mm respectively. The shoulder has convex scroll features and the pin has threaded feature to enhance the material flow. The tool rotational and traverse speeds for the FSS runs were 1000 rpm and 50 mm/min. respectively. All the runs were performed with the plunge depth of 1.8 mm.

The process responses such as the spindle torque, in-plane forces (x and y axes), forge force (z axis force) were acquired during the entire process cycle using a computer controlled system. The length of each FSS run was 50 mm for the cold sprayed coatings and 25 mm for the bare steel plate.

Fig. 3. Picture of the equipment used for FSS (picture at the inset is the FSS tool)

D. Sample Preparation for microstructure analysis

The samples for microstructure analysis were sectioned approximately at half the distance from the starting point of the FSS and the transverse section was used for the analysis. Fig. 4 shows the schematic of the FSS plate and the transverse view of the samples. The sectioned samples were mounted using the epoxy resin. The mounted samples were grinded using the silicon carbide abrasive papers, followed by the fine polishing using aluminum oxide particles. The final polishing was done using the diamond compound paste. The etching of the polished surface was done to reveal the microstructure of the steel samples. A chemical solution of 2 vol.% nitric acid in the distilled water was used for the chemical etching and the etching time was 5 to 10 s. The etched cross section was analyzed for microstructure and the micrographs were recorded using the image analyzer attached with the Leica light optical microscope.

E. Scanning Electron Microscopy (SEM) Analysis

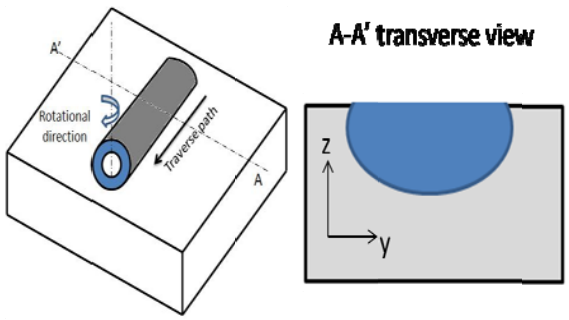

Fig. 4. Schematic of the FSS surface and the transverse section for microstructure analysis

The cross sections of differen FSS samples, as shown in figure 8 were analyzed in SEM for microstructure and the oxide particle analysis. The chemical composition of the CS layers and FSS zone was determined using the energy dispersive spectroscopy (EDS) attached with the SEM.

F. Microhardness Testing

Microhardness testing of the polished cross sections of the FSS samples was performed using the HWMMT–X7 Vickers microhardness tester. A load 50g and 10s dwelling time were used for indentation.

The hardness drop was run for the FSS samples at different depths from the top surface. The hardness drop is plotted as the hardness vs. distance from the top surface of the FSS zone along Z- axis.

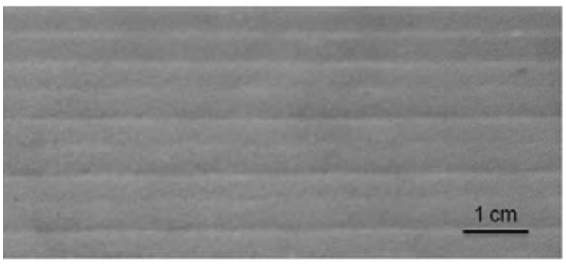

Fig. 5. The surface of the cold sprayed Zn-Y_2O_3-ZrO_2

III. RESULTS AND DISCUSSION

A. Cold sprayed coating appearance

Fig. 5 shows a portion of the cold sprayed Zn-Y_2O_3-ZrO_2 surface on the steel plate showing a banded appearance. The width of each band is equal to the width of the sprayed region created by a single run of the cold spray gun. The surface of the cold sprayed coating appears wavy with no visible discontinuities. The surface of the Cu/Y_2O_3-ZrO_2 coated steel plates also showed a similar appearance which is not shown in this manuscript.

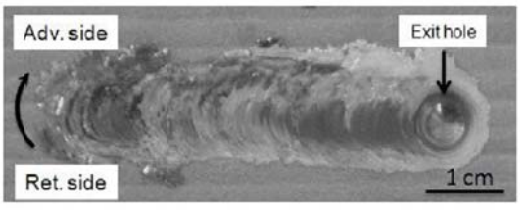

Fig. 6. The photo of the FSS surface of Zn-Y_2O_3-ZrO_2 cold sprayed coating

B. Surface Appearance of the FSS plates

Fig. 6 shows the FSS steel plate with the Zn-Y_2O_3-ZrO_2 cold sprayed layer. In figure 6 the side with an arrow indicates the start of the processing zone and the exit hole is the end of the FSS. The tool

rotational direction is indicated by the arrow (clockwise) and the traverse direction is from the left to the right of the image. The FSS surface is free from any discontinuities, showing loosely connected flash on the advancing side.

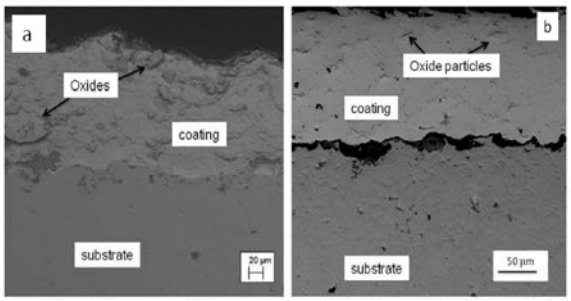

Fig. 7. SEM images of the as sprayed (a) Zn- Y_2O_3- ZrO_2 and (b) Cu-Y_2O_3-ZrO_2 coatings

C. Microstructure of the cold sprayed coatings

Fig. 7a and Fig. 7b show the backscattered electron image of the cross sections of the as cold sprayed Zn and Cu based cermets. The as sprayed Zn-Y_2O_3-ZrO_2 coating shows the dimples on the surface (Fig. 7a), whereas the waviness is relatively small in the Cu-Y_2O_3-ZrO_2 coatings (Fig.7b). The coatings do not show any visible pores inside the coating, however, the Cu-Y_2O_3-ZrO_2 coating shows visible pores, as black holes at the coating-substrate interface. The estimated area fraction of the Y_2O_3-ZrO_2 particles inside coating by the image analyzer is 27.45% and 16.4%, respectively for Zn-Y_2O_3-ZrO_2 and Cu-Y_2O_3-ZrO_2 coatings, respectively. The optimized cold spray parameters used in the present study has ensured > 10% oxide content inside the coatings. For a constant mass ratio (50:50), the oxide content in Zn-Y_2O_3-ZrO_2 is higher than that of the Cu-Y_2O_3-ZrO_2 layer, which may be correlated to the density difference in the feedstock particles. The density in g/cm^3 of Y_2O_3-ZrO_2, Zn and Cu is 6, 7.14 and 8.96, respectively. It is reasonable to presume that the small difference in density of Y_2O_3-ZrO_2 and Zn, and hence the particle velocity during cold spraying makes high Y_2O_3-ZrO_2 content in the Zn cermet coating. The deposition efficiency also depends on the initial particle size, shape and the impact velocity. The hard ceramic oxide particles make no bonding, only abrades with the substrate. However, when mixed with the ductile metals, it forms a coating by the 'wedging' and 'riveting' mechanism. At chosen velocity, kinetic energy of Cu-Y_2O_3-ZrO_2 particles is insufficient to penetrate inside the substrate surface by impact [3]. The hard, oxide particles in the feedstock require very high velocity to penetrate into the metal matrix. The plastically deformable metal forms a matrix with non-uniformly distributed separate oxide inclusions. Since, oxide particles cannot be plastically deformed; they are just mechanically interlocked inside the metal matrix [3]. The low oxide content in the Cu base coating can be explained using the above principle. The insufficient velocity can also be inferred from the large, visible pores at the coating-substrate interface (Fig.7b).

Fig. 7 also shows a significant difference in the particle size and distribution, in addition to its content. The particle number density, average area, average length and width of the particles inside the CS layers are presented in Table 4.

Table IV. Particle analysis results of the CS coatings

Coating	Number density	Area (□m^2)	length (□m)	width (□m)
Cu-Y_2O_3-ZrO_2	270	20.72	6.4	4.3
Zn-Y_2O_3-ZrO_2	97	115	14.6	9.2

Table 4 shows that in both the coatings, the defragmentation of the oxides during impact against the substrate at high velocity, as indicated by low average length and width of the oxide particles. The increased particle number density, low average length and width of the Cu-Y_2O_3-ZrO_2 coating compared to that of Zn-Y_2O_3-ZrO_2 indicates, a relatively, large degree of oxide defragmentation and or rebound of coarser Y_2O_3-ZrO_2 particles during the spray of Zn/-Y_2O_3-ZrO_2 coating.

D. Macrostructure of friction stir surfaced zones

Fig. 8 shows the pictures of friction stir surfaced cross sections of Cu-Y_2O_3-ZrO_2 (a) and Zn-Y_2O_3-ZrO_2 base (b) cold sprayed layers on the steel surface. In Fig. 8, left and right sides are respectively, the advancing and retreating sides. The advancing side is the side at which the tool rotation aids the material flow (directional vectors are of the same sign). The retreating side has the tool rotational and material flow vectors opposite to each other [6]. This asymmetry in the process leads to different strain and strain rate inside the stir zone and concomitant microstructural changes with respect to the centerline (dashed line in Fig.8). The FSS sections show no visible volumetric defects. The FSS results in breaking of the CS layer and pushing inside the stir zone as can be seen in Fig. 8b. As shown in figure 8, for similar rotational and traverse speeds, the stir zone size and shape for Zn-Y_2O_3-ZrO_2 CS layer is different from that of the Cu-Y_2O_3-ZrO_2 CS layer. After FSS, the Cu coated steel has developed a wider stir zone size (Fig.8a) than the Zn coated steel, which can be attributed to high thermal conductivity of the Cu (401 W/m.K) present in the Cu-Y_2O_3-ZrO_2 CS layer. In FSS, the maximum heat generation

occurs at the surface due to the friction between the tool and the workpiece (dissipation of plastic work) and resulting in maximum temperature at the surface. The generated heat is transferred in through thickness direction by conduction. It should be noted that the larger stir zone does not necessarily mean higher stir zone temperature.

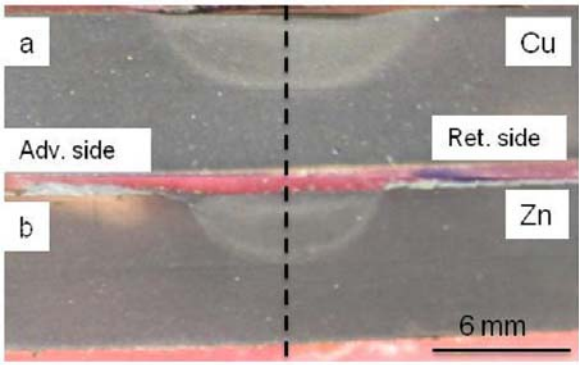

Fig. 8. Scanned cross sections of the stir zones of (a) Cu-Y_2O_3-ZrO_2 and (b) Zn-Y_2O_3-ZrO_2 coated steel

E. Torque, temperature and in-plane forces of FSS

The FSS experiments in the present work were performed using a constant plunge depth (position control mode). In this mode, the process response variables are the torque, in-plane forces, temperature (not measured in this work) and the resulting microstructure. The process response variables of the bare, Cu and Zn coated CS layers FSS are presented in Table 5.

Table V. Response variables of the FSS process

Type	F_z (kN)	Torque (N-m)	F_r (kN)
Bare	8.6	24.2	0.335
Cu-Y_2O_3-ZrO_2	15.7	21.2	1.06
Zn-Y_2O_3-ZrO_2	17.5	16.1	0.75

For similar rotational speed and feed rate, the forge force (F_z) required for consolidation of the cold sprayed coating is higher than that of the bare steel. It is reasonable to assume that presence of hard Y_2O_3-ZrO_2 particles in the cold sprayed coatings resulted in higher F_z levels compared to un-coated (bare) steel. The high F_z is used for consolidation and forging of the particles in the coating into the steel matrix. The average torque for the CS coatings is lower compared to that of the un-coated steel, indicating that stir zones of the CS coated steels are hotter than the un-coated steel. The stir zone temperature is inversely related to the average torque: high stir temperature leads to more softening of the material and the corresponding decrease in the torque levels [5]. Thus, in the absence of measured temperature data, experimentally acquired torque can be used to represent the stir zone temperature. The peak temperature during FSS can be estimated from the tool rotational and traverse speeds using following expression

$$\frac{T'}{T_m} = k\left[\frac{\omega^2}{v} \times 10^4\right]^{\alpha} \quad (1)$$

where T' is the temperature during welding (°C), T_m is the melting point of alloy (°C), ω is the tool rotational speed, v is the tool traversing speed, and α (~0.005) and K (~0.7) are constants. By substituting the values in above equation, the stir zone temperature is estimated to be 1390 K, which is above the upper critical temperature (AC_3=1158 K) of the steel substrate and the melting point of the Cu (1357.77 K) and Zn (692.68 K) present in the cold sprayed coatings [9]. High stir zone temperature results in the melting of the Cu and Zn followed by the solidification of the molten layer, forming an adherent layer with good bonding to the substrate steel. High temperature may also result in vaporization of significant amount of Zn (boiling point=1180K).

The temperature difference among the CS coated steels stir zone can be qualitatively obtained from the model equation proposed by Henrik and Hattel [10],

$$q_{total} = \omega\left[\delta\tau_{yield} + (1-\delta)\mu p\right] \quad (2)$$

In equation [2], q_{total} is the total heat generation in (W/m^2), □ is the angular velocity of the tool, r is the radial distance from the tool center, □ is the friction coefficient, p is the applied force, □ is the temperature dependent yield strength of the base metal and □ is the dimensionless slip rate between tool and the work piece. As per equation [2], the stir zone temperature is higher as the forge force (p) is increased and or the workpiece retains its strength at elevated temperature. Among the CS coatings, the magnitudes of the forge force ($p=F_z$) and strength of Zn base coating are higher compared to Cu base coating. Therefore, as per equation [2], the stir zone of the former is hotter than the latter. High stir zone temperature in CS Zn base coating resulted in low in-plane force as presented in Table 5. In FS process, the force in x-axis (F_x) is opposing the forward movement of the tool; the force in the y-axis (F_y) is the lateral force acting perpendicular to F_x and the z-axis force (F_z) is the vertical force in the plate thickness direction. The resultant force acting along the x-y coordinate frame is the net effect of the forces applied by the flow of material on the pin surface, which can be presented in 2D polar plots. In the polar plot, the magnitude of the resultant force, F_r is $(Fx^2+Fy^2)^{1/2}$ and theta (□) is the angle between the resultant force and the x-axis [11]. Fig. 9 shows the visualization of the in-plane forces around the tool

pin for the un-coated steel, Cu-Y_2O_3-ZrO_2 and Zn-Y_2O_3-ZrO_2 coated steels. The F_r distribution in the polar plot provides information about the material flow around the pin and defects, if any present inside the stir zone non-destructively. The magnitude and spread of the resultant force is related to the stir zone temperature. Fig. 9b (Cu base coating) shows a narrower spread in the force and higher magnitude of forces compared to Fig. 9c (Zn base coating). This indicates that stir zone temperature of the former is relatively lower compared to the latter.

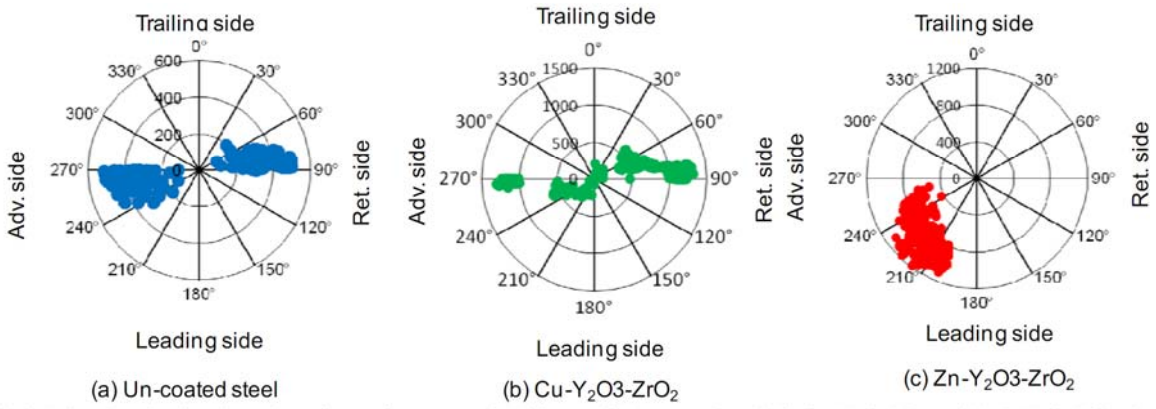

Fig. 9. Polar plots showing the resultant forces of representative FSS runs of (a) un-coated steel, (b) Cu- Y_2O_3-ZrO_2 and (c) Zn-Y_2O_3-ZrO_2 cold spray coated steels

F. Microstructure of the FSS zone

Fig. 10 shows the overview of microstructure of the FSS zone of steel with Cu-Y_2O_3-ZrO_2 layer. The stir zone exhibits a highly heterogeneous microstructure of distinct layers; 1) solidified top layer, 2) Fe and Cu composite layer, 3) banded region, 4) recrystallized zone and 5) martensitic region. High stir zone temperature resulted in the melting of the Cu and Zn in the cold sprayed cermet layers followed by the solidification of the molten layer on top of the substrate. The layer 2 in Fig. 10 is the composite layer of Cu, Fe and the oxides with very fine microstructure, which was not be revealed in the light optical microscopy. The FSS zone of Cu base layer shows the deformed band structure with alternate bands of the martensite and the ferrite+pearlite (region 3 in Fig. 10) The formation of banded region in the hot working is due to microsegregation of the alloying elements, particularly Mn, Si and Cr alloying elements [12]. The formation of banded region can also be attributed to threaded pin profile used for FSS [5]. In this study, variation in the concentration of the base metal constituent particles (Mn and Si) in the banded region (dark) is less significant; however, the phase transformation into a hard phase is evinced by the hardness measurement (refer section III). This indicates the presence of hard microstructural phase, perhaps martensite in the dark banded regions. The region 4 in Fig. 10 is the recrystallized ferrite and pearlite structure in the stir zone. The fine, ferrite and pearlite structure inside the stir zone indicates the recrystallization (R_x), where the R_x in the stir zone can be due to dynamic recrystallization (DRX) and or the static recrystallization which takes place during the cooling stage after the FSS [9]. High magnification optical micrographs of the stir zone are presented in Fig. 11. Fig. 11a shows the microstructure of the A387 steel substrate is bainitic with delineated prior austenitic grain boundaries. Fig. 11b shows the ferritic structure with some pearlitic grains. The ferrite and pearlite structure just below the composite layer inside the stir zone could be due to the low hardenability in this region caused by the contact with oxides present above the ferritic region.

The oxygen present in the ZrO_2 acts as the source of oxidation in the stir zone. The oxidation results in depletion of the hardenability improving elements like Cr, Mn, Mo etc., and thus resulting in non-martensitic transformation products [9]. The picture at the inset of Fig. 11b shows the dark martensite bands in the ferrite matrix. The layer below the ferritic region is composed of martensite with traces of the retained austenite (Fig.11c). The adiabatic heating and the dissipation of plastic work during FSP raises the stir zone temperature. For 1000 rpm and 50 mm/min traverse speed, the calculated stir zone temperature is 1390 K > upper critical transformation temperature (AC_3), which results in the austenization of bainite in the base metal.

The austenization is followed by the solid- state transformation into martensite inside the stir zone with the evident of retained austenite (Fig.11c). The cooling rate at any point inside the stir zone behind the traversing tool can be calculated using the Rosenthal equation [13], which assumes a moving point source of the heat at the origin of a moving reference frame and considers heat flow only by conduction.

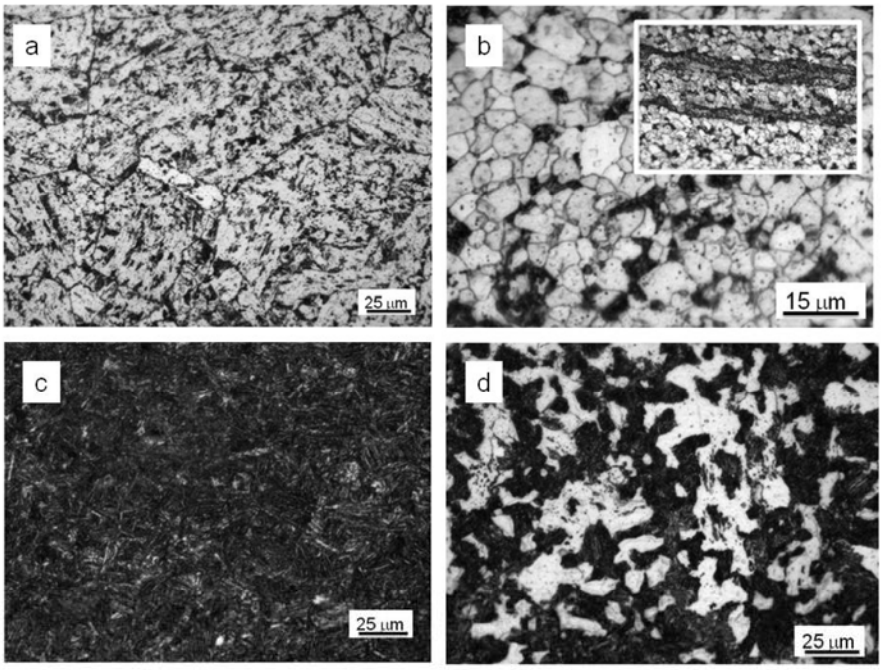

Fig. 11. Optical micrographs of (a) steel substrate, (b) ferrite and pearlite soft zone and martensite bands in ferrite at the inset, (c) martensite inside the stir zone and (d) martensite and ferrite in thermo-mechanically affected zone inside FSS of steel with Cu-Y_2O_3-ZrO_2 cold sprayed layer

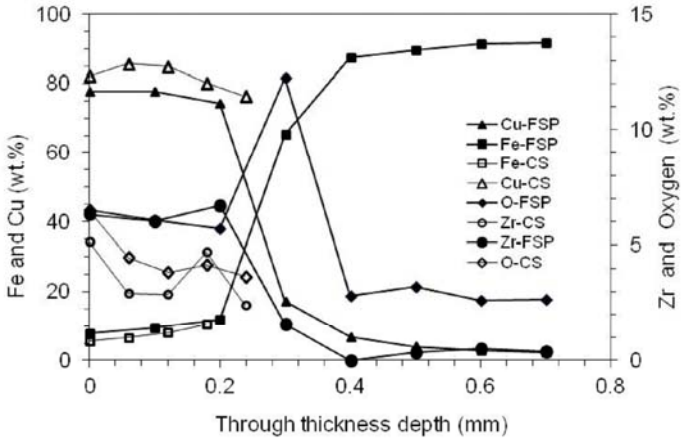

Fig. 12. Composition profile comparison before and after the friction stir surfacing of the cold sprayed steel

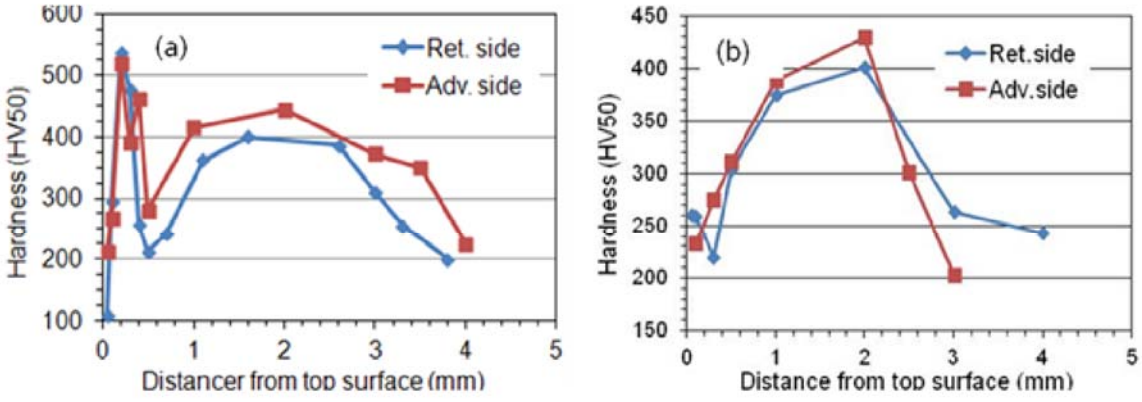

Fig. 13. Hardness drop inside the stir zone of (a) Cu-Y_2O_3-ZrO_2 and (b) Zn-Y_2O_3-ZrO_2 cold sprayed steel surfaces

$$\frac{\partial T}{\partial t} = -2\pi k \frac{(T - T_0)^2}{\left(\frac{Q}{V}\right)} \quad (3)$$

By substituting the traverse speed (v), measured power (Q) from the experiments and appropriate thermal conductivity (k), the cooling rate from the peak temperature to M_s is 8°C/s. The actual cooling rate is however > 8°C/s due to the presence of highly conductive Zn and Cu layers which acts as the heat sink and dissipates the heat through the top surface by conduction. The tendency of steel for martensitic transformation can be better explained based on the cooling rate, maximum times necessary for fully martensite transformation i.e., M_s from the peak 1360K to 660K temperature t_M (s) and the minimum times for no martensite transformation t_B (s). The t_M, t_B and the time between 1360 K and 660K is 0.15s, 97s and 88s, respectively [14]. This indicates that the cooling rate at the wake of the traversing tool is high enough to results in martensitic structure in the stir zone. The cooling rate at the adjacent regions of the stir zone (TMAZ and HAZ) perhaps lower (due to high temporal length of the temperature transient) than that of the critical cooling resulting in mixture of ferrite and martensite the TMAZ and ferrite+pearlite region at HAZ regions.

G. SEM and elemental analysis results

Fig. 12 shows the composition profile obtained from the SEM, energy dispersive spectroscopy (EDS) analysis of the Cu-Y_2O_3-ZrO_2 cold sprayed layer and the corresponding friction stir zone. The open and closed symbols correspond to before and after the stir processing, respectively. The stir zone shows the presence of metallic Fe (squares) of average 10 wt.% up to 0.2 mm and an abrupt increase in the content towards the substrate, as expected. The Zr (circles) and Cu (triangles) profiles exhibit almost a plateau up to 0.2 mm and then starts declining in similar trends with distance up to 0.4 mm. The profile becomes plateau beyond 0.4 mm. The oxygen profile is similar to Zr and Cu up to 0.2 mm and exhibiting a local maximum in the profile. Based on the composition profile, an effective thickness of the processed zone is 0.4 mm. Fig. 12 shows that the composition profile (Fe, Zr, Cu and oxygen) of the cold sprayed layer has relatively larger compositional variation (open symbols) compared to friction stir surfaced zone (closed symbols). This is due to the homogenization of the elements in the cold sprayed layer by friction stir surfacing. Also, the average Fe (wt.%) value in the stir zone is greater than that of as sprayed zone, which is due to the upward movement of Fe from the substrate by the tool action. In FSS, the tool shoulder and threaded features in the pin tool enhance the churning of the particles in through thickness direction, and the degree of churning is more at the top surface. For a pin diameter of 5 mm, tool rotational speed of 1000 rpm and 50 mm/min traverse speed, the true strain value as per the model proposed by A.P. Reynolds [15] is 10.59 and the corresponding strain rate ($\dot{\varepsilon}$) is calculated as $3.5s^{-1}$.

During FSS, the ductile steel matrix can withstand the true strain of 10.59, but Y_2O_3-ZrO_2 particles in the CS layer cannot accommodate the high strain values generated during FSS. This eventually leads to comminution of the oxide particles inside the stir zone, particularly in the molten, densified friction stir processed layer. Table 6 shows the comparison of particles data for the Cu-Y_2O_3-ZrO_2 CS and FSS structures of the steel. The reduction in the volume fraction of the particles in the FSS layer compared to the CS layer is attributed to the material loss in the flash produced during FSS. The particle analysis results indicate that the FSS of the CS layer results in the comminution of the oxide particles by virtue of severe deformation and the uniform material flow caused by the profiled FSS tool.

Table VI Particle Analysis Results of the CS and FSS

Sample	Area fraction (%)	Particles number density	Avg. Particle area (μm^2)
CS Cu-Y_2O_3-ZrO_2	16.4	307	4
FSS Cu-Y_2O_3-ZrO_2	11.6	263	2.6

H. Microhardness of the CS and FSS zones

The microhardness drop from surface through plate thickness of the stir zone is shown in Fig. 13. The hardness drop of Cu-Y_2O_3-ZrO_2 and Zn- Y_2O_3-ZrO_2 cold sprayed and friction stir surfaced steels presented in Fig. 13a and Fig.13b, respectively. The x and y axes of the plots represent the distance from the top surface and the hardness values, respectively. The hardness profile of both Cu (Fig. 13a) and Zn (Fig.13b) coated steel stir zones exhibit a dip around 0.4 mm and again increases beyond 0.4 mm. The dip in the hardness corresponds to the softer region (ferrite+pearlite) inside the stir zone and increasing hardness beyond 0.4 mm is due to the martensitic structure. The average hardness at the top solidified layer (at .05 mm from the top surface) is 157±47 HV and 259±31 HV, respectively for the Cu-Y_2O_3-ZrO_2 and Zn-Y_2O_3-ZrO_2 (at 0.1 mm from the top surface) friction stir surfaced layers, respectively. The lower hardness of the latter coating compared to the former is due to the high area % of Y_2O_3-

ZrO_2present in the Zn cermet coating. The peak hardness value in Fig.13a corresponds to the dark composite layer present in the Cu-Y_2O_3-ZrO_2 coated steel stir zone (Fig.10) which is composite structure of Cu, Fe, oxides with some martensite. The local minimum hardness at 0.5 mm in Fig. 13a corresponds to the ferritic region in the recrystallized zone. The hardness value rises again after 0.5 mm as it approaches the martensite. Further decline in hardness beyond 3 mm is corresponding to heat affected zone and finally reaching the values of the base metal, i.e., > 200 HV on an average. The Zn-Y_2O_3-ZrO_2 coating demonstrated higher hardness (259±31 HV) values at the top layer compared to that of the base metal, due to the presence of the hard oxides inside the layer. The peak hardness in the stir zone is shifted to the martensitic region at a distance of 0. 2 mm from the top surface.

IV. CONCLUSION

Friction stir surfacing of the cold sprayed metal-oxides coated steel surfaces resulted in the formation of dense, pore free adherent composite layer on the steel surface. The closing of pores present at the coating-substrate interface, which should improve the adhesion strength. The stir zone demonstrates a well mixing between the cold sprayed particles and the substrate iron, but no intermetallic compounds were formed, which is beneficial in terms of the toughness. In summary, the cold spraying and friction stir surfacing can be considered in combination to produce defect free functional surface composite for engineering applications. Process parameters optimization and careful selection of reinforcement particles are recommended for specific applications.

ACKNOWLEDGEMENT

The authors thank Dr. Thomas Grandke, Materials-Technology Field, Siemens AG, Germany for the financial support. The authors thank Mr. Mr. Vidyabhushana Hande, Head, CT RTC AUC ASO-IN and for his guidance and inputs in preparation of this manuscript. Thanks to Mr. Deepak Bhandari, Intellectual Property Department and Mr. Ramesh Viswanathan, Head, Technology and Innovation Management, Siemens Technology and Services, Pvt. Ltd., Bangalore for permission to publish this work. The support of Dr. S. Kumar, ARCI Hyderabad, Dr. Tapan Kumar Pal and Rajarshi Sarkar of Jadavpur University, Kolkata for experiments and consultancy are greatly acknowledged.

REFERECES

[1] X. Ning, J. Jang nd H. Kim, “The effects of powder properties on in-flight particle velocity and deposition process during low pressure cold spray process,” Applied Surface Science, vol.253, pp. 7449-7455, March 2007.

[2] V.F. Kosarev, S.V. Klinkov and A.A. Sova, “Recently Patented Facilities and Applications in Cold Spray Engineering,” Recent Patents on Engineering, vol. 1, no. 1, pp. 33-42, 2007.

[3] A. Sova, V.F. Kosarev, A. Papyrin, and I. Smurov, “Effect of ceramic particle velocity on cold spray deposition of metal-ceramic coatings,” Journal of Thermal Spray Technology, vol. 20, no.1-2, pp. 285-291, January 2011.

[4] J. Karthikeyan, Cold spray technology: International status and USA efforts, ASB Industries Inc. USA, December 2004.

[5] P. Venkateswaran and A.P. Reynolds, “Factors affecting the properties of friction stir welds between aluminium and magnesium alloys”, Materials science and engineering A, vol. 545, pp. 26-37, March 2012.

[6] R.S. Mishra and Z.Y. Ma, “Friction stir welding and processing”, Materials Science and Engineering:R: Reports, vol. 50, nos. 1-2, pp. 1-78, August 2005.

[7] P.B. Berbon, W.H. Bingel, R.S. Mishra, C.C. Bampton and M.W. Mahoney, “Friction stir processing: a tool to homogenize nanocomposite aluminum alloys”, Scripta materialia, vol. 44, no.1, pp. 61-66, August 2000.

[8] S.J. Bailey,N.C. Baldini, Annual Book of ASTM Standards, ASTM International, West Conshohocken, PA, 2007.

[9] M. Ghosh, K. Kumar and R.S. Mishra, “Analysis of microstructural evolution during friction stir welding of ultrahigh-strength steel,” Scripta Materialia, vol. 63, pp. 851–854, August 2010.

[10] H.B. Schmidt and J.H. Hattel, “Thermal modelling of friction stir welding,” Scripta Materialia, vol. 43, no.5, pp. 332-337, August 2008.

[11] N. Balasubramanian, B. Gattu and R. S. Mishra, “Process forces during friction stir welding of aluminium alloys,” Science and technology of welding and joining, vol. 14, no. 2, pp. 141-145, 2009.

[12] S.E. Offerman, N.H. van Dijk, M.Th. Rekveldt, J. Sietsma, S.M. van der Zwaag, “Ferrite/pearlite band formation in hot rolled medium carbon steel,” Materials Science and Technology, vol. 18, no. 3, pp.297-303, March 2002.

[13] S. Swaminathan, K. oh-ishi, A.P. Zhilyaev, C.B. Fuller, B. London, M.W. Mahoney and T.R. Mcnelley, “Peak Stir Zone Temperatures during Friction Stir Processing,” Metallurgical and Materials Transactions A, vol. 41, no. 3, pp. 631-640, March, 2010.

[14] M. Matsushita, Y. Kitani, R. Ikeda, M. Ono, H. Fujii and Y.-D. Chung, “Development of friction stir welding of high strength steel sheet,” Science and Technology of Welding and Joining, vol.16, no.2, pp. 181-187, 2011.

[15] A.P. Reynolds, “Flow visualization and simulation in FSW”, vol. 58, no.5, pp. 338-342, March 2008.